UNIVERSITY
OF TRENTO

DIPARTIMENTO DI INGEGNERIA E SCIENZA DELL'INFORMAZIONE

38123 Povo – Trento (Italy), Via Sommarive 14
http://www.disi.unitn.it

A NEW METHODOLOGY BASED ON AN ITERATIVE MULTI-SCALING FOR MICROWAVE IMAGING

S. Caorsi, M. Donelli, D. Franceschini and A. Massa

April 2003

Technical Report # DISI-11-007

A New Methodology Based on an Iterative Multi-scaling for Microwave Imaging

Salvatore Caorsi*, *Member, IEEE*, Massimo Donelli**, Davide Franceschini*** and Andrea Massa***, *Member, IEEE*

* Department of Electronics,

University of Pavia, Via Ferrata 1, 27100 Pavia - Italy

Tel. +39 0382 505661, Fax +39 0382 422583, E-mail: *caorsi@ele.unipv.it*

** Department of Biophysical and Electronic Engineering,

University of Genoa, Via Opera Pia 11/A, 16145 Genoa - Italy

Tel. +39 010 3532796, Fax +39 010 3532245, E-mail: *donelli@dibe.unige.it*

*** Department of Information and Communication Technology,

University of Trento, Via Mesiano 77, 38050 Trento - Italy

Tel. +39 0461 882057, Fax +39 0461 881696, E-mail: *andrea.massa@ing.unitn.it*

A New Methodology Based on an Iterative Multi-scaling for Microwave Imaging

Salvatore Caorsi*, *Member, IEEE*, Massimo Donelli**, Davide Franceschini*** and Andrea Massa***, *Member, IEEE*

Abstract

In this work the problem of the localization, shaping and dielectric permittiviy reconstruction of dielectric targets is addressed. The scatterers under test are inhomogeneous cylinders of arbitrary cross sections probed by a set of incident electromagnetic fields of TM type. The scattered field data are processed in order to locate and roughly recover the objects' shapes. Then the scatterers under test are reconstructed with an increasing accuracy by means of an iterative multi-scaling procedure until stationary reconstructions are achieved. The proposed method is presented jointly with a modified conjugate-gradient inversion procedure in order to minimize the arising cost function. However, this methodology is independent from the minimization algorithm and other and more efficient algorithms can be used. In order to assess the effectiveness of the iterative multi-scaling method, the results of several test cases (with and without noise) are presented and discussed in more detail.

Index Terms - Microwave imaging, inverse scattering, iterative multi-scaling method.

1 Introduction

The problem of the localization and the dielectric reconstruction of unknown targets from the measurement of the scattered field is a topic of great interest in the framework of microwave imaging techniques (see [13] and the references therein) based on inverse scattering methodologies [1]-[3]. Moreover, many problems occurring in various areas of applied science, such as biomedical engineering [5], medicine [6][7], non destructive testing for the industrial production [8], buried objects detection and reconstruction [9]-[11] can be mathematically formulated as inverse scattering problems (see [12] for a complete overview). However, severe limitations in obtaining accurate reconstructions are due to some intrinsic drawbacks of the inverse scattering problem [14], [15] jointly with the feasibility of efficient illumination and measurements systems.

By a mathematical point of view, three main topics must be preliminary addressed in order to define an efficient reconstruction procedure: the uniqueness of the solution, the ill-posedness and the intrinsic nonlinearity of the problems. As far as the uniqueness is concerned, the dielectric profile of the object under test results uniquely defined only if pressing requirements (very difficult to be achieved in real situations) are verified [16], [17]. Generally speaking, the non-uniqueness and the ill-posedness drawbacks of the inverse problem are due to the limited amount of information that can be collected. In fact the number of independent data achievable from the measurements of the scattered field is essentially limited [24]. It leads to the conclusion that the space of the unknown is of finite dimension and consequently only a finite number of parameter of the unknown contrast can be accurately retrieved.

In order to recover a solution of the inverse scattering problem, a generalized solution is then defined by searching for approximate solutions satisfying additional constraints coming from the physics of the problem. This additional information is necessary in order to compensate the loss of information due to the imaging process [25]. To this end, a suitable cost functional is defined, whose global minimum is assumed as the reconstructed

profile.

On the other hand, due to the multiple scattering phenomena, the inverse scattering problem results nonlinear [15] as well as the arising cost function. The nonlinearity can be avoided for a certain limited real cases for which a linear relationship between the scattered field and the object under test can be found [18]. However, when multiple scattering effects is not negligible as is the case for large or highly contrasted objects, the use of nonlinear methodologies is mandatory. A lot of very effective optimization strategies have been proposed. These techniques can be grouped into deterministic (e.g., the modified gradient approach [19] or the distorted-Born iterative method [20]) or stochastic methods (e.g., the simulated-annealing procedure [21] or the genetic-algorithm based approaches [22]).

This paper presents a method located in the framework of optimization techniques and aimed at better exploiting all the available information. Analogously to standard optimization techniques, the proposed methodology uses the additional information (expressed in form of constraints on the solution) at the start of the iterative procedure to construct approximate solutions. But successively the procedure iterates a sort of zoom inside the investigation domain introducing a sort of "acquired" information about the scatterer under test (information achieved at the previous reconstruction steps). That helps to locate the scatterer inside the investigation domain and at the same time to reallocate all the available a-priori information in order to achieve a finer reconstruction.

In the next sections the proposed technique will be widely illustrated. After the mathematical statement of the problem and an analytical description of the iterative multi-scaling procedure (Section 2), some numerical experiments will be shown in Sec. 3. Dielectric scatterers various in shapes, dimensions and permettivities will be considered in order to accurately evaluate current potentialities of the proposed method. Finally (Section 4) some conclusions will be drawn and possible future developments pointed out.

2 Mathematical Formulation

Let us consider a cylindrical object belonging to an investigation domain, D (Figure 1). The target is illumined by a finite set of incident electromagnetic fields of TM type ($\mathbf{E}^v_{inc}(\mathbf{r}) = E^v_{inc}(x,y)\hat{\mathbf{z}};\ v = 1,...,V$). The scattered electric field is collected at $M^{(v)}$ different measurement points, located in an observation domain, D_{obs}, external to the investigation domain ($\mathbf{E}^v_{scatt}(\mathbf{r}) = E^v_{scatt}(x_{m_{(v)}}, y_{m_{(v)}})\hat{\mathbf{z}};\ m_{(v)} = 1,...,M^{(v)}$).

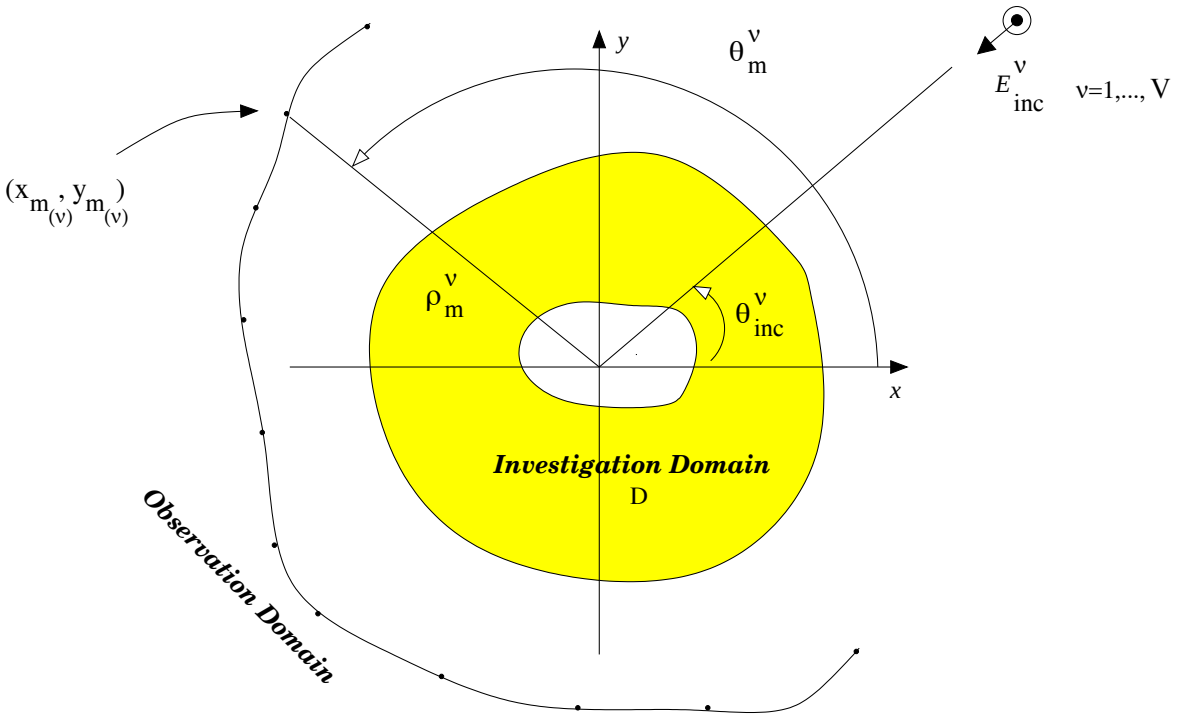

Figure 1. Imaging configuration.

The material properties of the dielectric object are modeled by means of an object function $\tau(x,y)$ defined as follows

$$\tau(x,y) = \varepsilon_r(x,y) - 1 - j\frac{\sigma(x,y)}{2\pi f \varepsilon_0} \tag{1}$$

being $\varepsilon_r(x,y)$ and $\sigma(x,y)$ the dielectric permittivity and the electric conductivity, respectively. A lossless non-magnetic background medium, characterized by a dielectric per-

mittivity ε_0, is assumed. The interactions between scatterer and probing electromagnetic fields are described by means of the inverse scattering equations [26]

$$E^v_{scatt}(x_{m_{(v)}}, y_{m_{(v)}}) = j\frac{k_0^2}{4}\int\int_D \tau(x',y')E^v_{tot}(x',y')H_0^{(2)}(k_0\rho_{m_{(v)}})dx'dy' \quad (x_{m_{(v)}}, y_{m_{(v)}}) \in D_{obs}$$
$$m_{(v)} = 1, ..., M^{(v)}$$
$$v = 1, ..., V \tag{2}$$

$$E^v_{inc}(x,y) = E^v_{tot}(x',y') + j\frac{k_0^2}{4}\int\int_D \tau(x',y')E^v_{tot}(x',y')H_0^{(2)}(k_0\rho)dx'dy' \quad (x,y) \in D$$
$$v = 1, ..., V \tag{3}$$

where k_0 is the background wave number, and $H_0^{(2)}$ is the $0th$ second kind Hankel function being $\rho_{m_{(v)}} = \sqrt{\left(x - x_{m_{(v)}}\right)^2 + \left(y - y_{m_{(v)}}\right)^2}$ and $\rho = \sqrt{(x-x')^2 + (y-y')^2}$. In order to numerically solve the addressed inverse scattering problem, equations (2)-(3) are discretized according to the well-known Richmond's procedure [27]. The investigation domain D is discretized into N square subdomains. The electric field and the object function are constant quantities in each subdomain and equal to $E^v_{tot}(x_n, y_n)$ and $\tau(x_n, y_n)$, respectively. Then, the following algebraic system is obtained

$$E^v_{scatt}\left(x_{m_{(v)}}, y_{m_{(v)}}\right) = \sum_{n=1}^{N}\left\{\tau(x_n,y_n)E^v_{tot}(x_n,y_n)G_{2d}\left(\rho_{nm_{(v)}}\right)\right\} \quad m_{(v)} = 1, ..., M^{(v)} \tag{4}$$

$$E^v_{inc}(x_n,y_n) = E^v_{tot}(x_n,y_n) + \sum_{q=1}^{N}\left\{\tau(x_q,y_q)E^v_{tot}(x_q,y_q)G_{2d}(\rho_{nq})\right\} \quad n = 1, ..., N \tag{5}$$

where

$$G_{2d}\left(A_q, \rho_{nq}\right) = \left\{ \begin{array}{ll} \left(\frac{j}{2}\right)\left[k_0\sqrt{A_q\pi}H_1^{(2)}\left(k_0\sqrt{\frac{A_q}{\pi}}\right) - 2j\right] & if\ p = n \\ \frac{jk_0\sqrt{A_q\pi}}{2}H_0^{(2)}\left(k_0\rho_{nq}\right)J_1\left(k_0\sqrt{\frac{A_q}{\pi}}\right) & otherwise \end{array} \right\} \tag{6}$$

$$G_{2d}\left(A_n, \rho_{nm_{(v)}}\right) = \frac{jk_0\sqrt{A_n\pi}}{2}H_0^{(2)}\left(k_0\rho_{nm_{(v)}}\right)J_1\left(k_0\sqrt{\frac{A_n}{\pi}}\right) \tag{7}$$

being $H_1^{(2)}$ first-order Hankel function of the second kind, J_1 the Bessel function of second kind, and A_n the area of nth sub-domain.

Generally, in order to obtain a solution of the arising multi-objective problem, a suitable

cost function is defined as follows

$$\Phi\left\{\tau\left(x_n,y_n\right),E_{tot}^{v}\left(x_n,y_n\right);\,n=1,...,N;\,v=1,...,V\right\}=$$
$$\left\{\sum_{v=1}^{V}\sum_{m=1}^{M}\left|E_{scatt}^{v}\left(x_{m_{(v)}},y_{m_{(v)}}\right)-\sum_{n=1}^{N}\left\{\tau\left(x_n,y_n\right)E_{tot}^{v}\left(x_n,y_n\right)G_{2d}\left(A_n,\rho_{nm_{(v)}}\right)\right\}\right|^2\right\}+$$
$$\left\{\sum_{v=1}^{V}\sum_{n=1}^{N}\left|E_{inc}^{v}\left(x_n,y_n\right)-\left[E_{tot}^{v}\left(x_n,y_n\right)+\sum_{q=1}^{N}\left\{\tau\left(x_q,y_q\right)E_{tot}^{v}\left(x_q,y_q\right)G_{2d}\left(A_q,\rho_{nq}\right)\right\}\right]\right|^2\right\} \tag{8}$$

and successively minimized according to an optimization strategy [29], [30], [31], [32].

The proposed methodology is independent from the definition of the cost function and also from the minimization algorithm. The method is aimed at better resolving the object function distribution by considering a multi-resolution iterative process. At the first step of the of the inversion procedure ($s=1$), a "coarse" profile of the object function distribution is looked for and the same resolution level, $R=1$ (being R the index of the resolution level), is considered in any part of the investigation domain. Then, on the basis of the first reconstruction, a "zoom" (by using the *acquired a-priori information* about the scenario under test) is performed in the region where the unknown scatterer has been detected. Iteratively the procedure is repeated until a "stationary" reconstruction is achieved.

In more detail, at each step of the iterative process, by means of the *acquired a-priori information* (achieved at the previous steps), the scatterer under test is localized and a zoomed square investigation domain, $D_{(s-1)}$, centered at

$$\begin{aligned} x_{c_{(s-1)}} &= \frac{\sum_{r=1}^{R}\sum_{n_{(r)}=1}^{N_{(r)}}\left\{x_{n_{(r)}}\,\tau\left(x_{n_{(r)}},y_{n_{(r)}}\right)\right\}}{\sum_{n_{(r)}=1}^{N_{(r)}}\left\{\tau\left(x_{n_{(r)}},y_{n_{(r)}}\right)\right\}} \qquad R=s-1 \\ y_{c_{(s-1)}} &= \frac{\sum_{r=1}^{R}\sum_{n_{(r)}=1}^{N_{(r)}}\left\{y_{n_{(r)}}\,\tau\left(x_{n_{(r)}},y_{n_{(r)}}\right)\right\}}{\sum_{n_{(r)}=1}^{N_{(r)}}\left\{\tau\left(x_{n_{(r)}},y_{n_{(r)}}\right)\right\}} \end{aligned} \tag{9}$$

$L_{(s-1)}$ in side,

$$L_{(s-1)}=2\frac{\sum_{r=1}^{R}\sum_{n_{(r)}=1}^{N_{(r)}}\left\{\frac{\rho_{n_{(r)}c_{(s-1)}}\,\tau\left(x_{n_{(r)}},y_{n_{(r)}}\right)}{max_{n_{(r)}=1,..,N_{(r)}}\left\{\tau\left(x_{n_{(r)}},y_{n_{(r)}}\right)\right\}}\right\}}{\sum_{r=1}^{R}\sum_{n_{(r)}=1}^{N_{(r)}}\left\{\frac{\tau\left(x_{n_{(r)}},y_{n_{(r)}}\right)}{max_{n_{(r)}=1,..,N_{(r)}}\left\{\tau\left(x_{n_{(r)}},y_{n_{(r)}}\right)\right\}}\right\}} \tag{10}$$

is defined, being $\left(x_{n_{(r)}}, y_{n_{(r)}}\right)$ the center of the square sub-domain ($l_{(r)}$-sided). According to a multi-resolution strategy, an higher resolution level ($R = s$) is adopted only for the reduced investigation domain. $D_{(s-1)}$ is discretized in N_R square sub-domain l_r-sided ($l_r < l_{(r-1)}$). The number of discretization domains is chosen equal to the essential dimension of the scattered data. The up-graded permittivity profile is then retrieved by minimizing the multi-resolution cost function, $\Phi^{(s)}$, defined as follows:

$$\begin{aligned}\Phi^{(s)}\left\{\tau\left(x_{n_{(r)}}, y_{n_{(r)}}\right), E^v_{tot}\left(x_{n_{(r)}}, y_{n_{(r)}}\right); r = 1, ..., R = s; n_{(r)} = 1, ..., N_{(r)}; v = 1, ..., V\right\} = \\ \left\{\sum_{v=1}^{V}\sum_{m=1}^{M}\left|E^v_{scatt}\left(x_{m_{(v)}}, y_{m_{(v)}}\right) - \sum_{r=1}^{R}\sum_{n_{(r)}=1}^{N_{(r)}}\left\{w\left(x_{n_{(r)}}, y_{n_{(r)}}\right)\tau\left(x_{n_{(r)}}, y_{n_{(r)}}\right)\right.\right. \\ \left.\left. E^v_{tot}\left(x_{n_{(r)}}, y_{n_{(r)}}\right) G_{2d}\left(A_{n_{(r)}}, \rho_{n_{(r)}m_{(v)}}\right)\right\}\right|^2\Bigg\} + \Bigg\{\sum_{v=1}^{V}\sum_{r=1}^{R}\sum_{n_{(r)}=1}^{N_{(r)}} \\ \left\{w\left(x_{n_{(r)}}, y_{n_{(r)}}\right)\left|E^v_{inc}\left(x_{n_{(r)}}, y_{n_{(r)}}\right) - \left[E^v_{tot}\left(x_{n_{(r)}}, y_{n_{(r)}}\right)\right.\right.\right. \\ \left.\left.\left. + \sum_{q_{(r)}=1}^{N_{(r)}}\left\{\tau\left(x_{q_{(r)}}, y_{q_{(r)}}\right) \quad E^v_{tot}\left(x_{q_{(r)}}, y_{q_{(r)}}\right) G_{2d}\left(A_{q_{(r)}}, \rho_{q_{(r)}n_{(r)}}\right)\right\}\right]\right|\Bigg\}^2\Bigg\}\end{aligned} \tag{11}$$

where, w, is a weighting function

$$w\left(x_{n_{(r)}}, y_{n_{(r)}}\right) = \begin{cases} 0 \quad if \quad \left(x_{n_{(r)}}, y_{n_{(r)}}\right) \notin D_{(s-1)} \\ 1 \quad if \quad \left(x_{n_{(r)}}, y_{n_{(r)}}\right) \in D_{(s-1)} \end{cases} \tag{12}$$

and $A_{n_{(r)}} = \left(l_{(r)}\right)^2$ is the area of the nth cell at the Rth resolution level.

The multi-resolution procedure is iterated until a "stationary condition" for the quantitative imaging of the scatterer under test is achieved ($s = S_{opt}$). This condition hold when

$$\eta_x^{(s)} = \left\{\frac{\left|x_c^{(s+1)} - x_c^{(s)}\right|}{\left|x_c^{(s+1)}\right|} \times 100\right\} < \eta_x \tag{13}$$

$$\eta_y^{(s)} = \left\{\frac{\left|y_c^{(s+1)} - y_c^{(s)}\right|}{\left|y_c^{(s+1)}\right|} \times 100\right\} < \eta_y \tag{14}$$

and

$$\eta_L^{(s)} = \left\{\frac{\left|L_{(s+1)} - L_{(s)}\right|}{L_{(s+1)}} \times 100\right\} < \eta_L \tag{15}$$

. Figure 2 summarizes the iterative multi-resolution procedure by means of a pictorial representation.

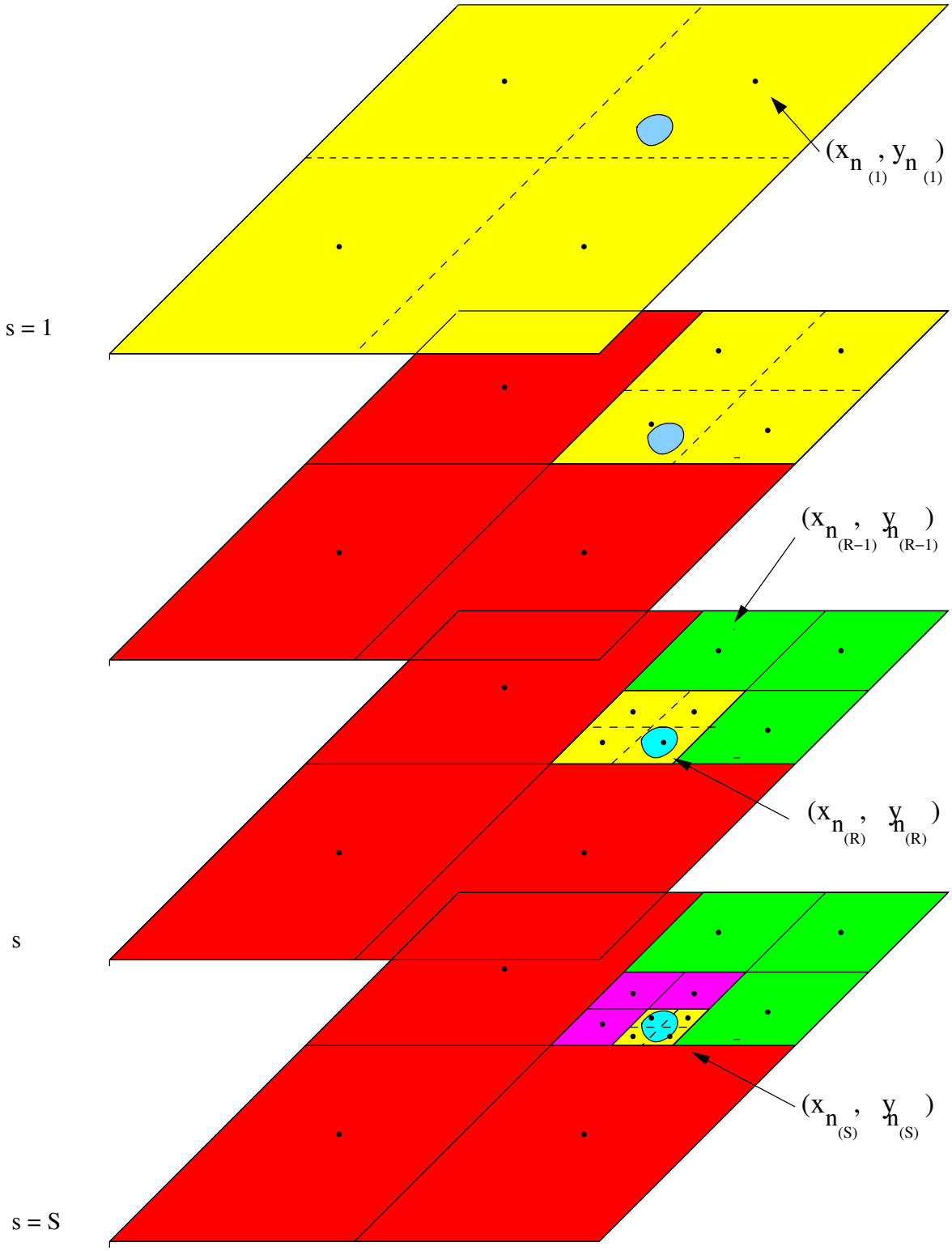

Figure 2. Iterative Multi-Resolution Schema.

3 Numerical Results

In this section, in order to asses the effectiveness of the proposed method, the results of several numerical simulations are reported. The behavior of the proposed method is illustrated by considering three different class of scatterers: irregular homogeneous scatterers, circular homogeneous scatterers, and inhomogeneous scatterers.

3.1 Definitions

Before presenting the set of illustrative test cases, some quantities, used in the numerical analysis, are defined. In order to evaluate the local and global reconstruction accuracy, let us consider the following error figures

$$\gamma_{(j)} = \sum_{r=1}^{R} \frac{1}{N_{(r)}^{(j)}} \sum_{n_{(r)}=1}^{N_{(r)}^{(j)}} \left\{ \frac{\tau(x_{n_{(r)}}, y_{n_{(r)}}) - \tau^{ref}(x_{n_{(r)}}, y_{n_{(r)}})}{\tau^{ref}(x_{n_{(r)}}, y_{n_{(r)}})} \right\} \times 100 \qquad R = S_{opt} \tag{16}$$

where τ and τ^{ref} are the values of the actual and reconstructed object function, respectively; $N_{(r)}^{(j)}$ can range over the whole investigation domain ($j \Rightarrow tot$), or over the area where the actual scatterer is located ($j \Rightarrow int$), or over the background belonging to the investigation domain ($j \Rightarrow ext$).

Moreover, let us define the "*local error*"

$$\chi_{n_{(r)}} = \frac{\left| \tau(x_{n_{(r)}}, y_{n_{(r)}}) - \tau^{ref}(x_{n_{(r)}}, y_{n_{(r)}}) \right|}{\left| \tau^{ref}(x_{n_{(r)}}, y_{n_{(r)}}) \right|} \times 100 \tag{17}$$

for each discretization cell of the investigation domain.

As far as the assessment of the effectiveness in the qualitative imaging of the geometry under test is concerned, the following parameters are defined

$$\rho = \frac{\sqrt{\left[x_c^{(S_{opt})} - x_c^{ref}\right]^2 + \left[y_c^{(S_{opt})} - y_c^{ref}\right]^2}}{\lambda_0} \tag{18}$$

$$\Delta = \left\{ \frac{L_{(S_{opt})} - L_{ref}}{L_{ref}} \right\} \times 100 \tag{19}$$

The presence of a noisy environments is also taken into account by considering an additive Gaussian noise characterized by a signal-to-noise ratio defined as follows

$$SNR = 10log \left\{ \frac{\sum_{v=1}^{V} \sum_{m=1}^{M} \left| E_{scatt}^{v} \left(x_{m_{(v)}}, y_{m_{(v)}} \right) \right|^2}{\sum_{v=1}^{V} \sum_{m=1}^{M} \left| \mu \left(x_{m_{(v)}}, y_{m_{(v)}} \right) \right|^2} \right\} \tag{20}$$

being μ a complex gaussian random variable with zero mean value.

3.2 Homogeneous Square Cylinder

In the first example, a lossless square scatterer $L = 0.8\,\lambda_0$-sided, belonging to an inaccessible square investigation domain ($L_D = 2.4\,\lambda_0$), is located at $x_c^{ref} = -y_c^{ref} = 0.4\,\lambda_0$. The object is characterized by an homogeneous distribution of the object function $\tau = 0.5 + j0.0$ (Fig. $3(a)$). A set of $V = 4$ unit TM plane waves (whose incident angles are given by $\theta_{inc}^{v} = (v-1)\frac{\pi}{2}$, $v = 1, ..., V$) illuminated the investigation domain. For each illumination, the scattered electric field data have been collected at $M = 21$ equally-spaced detectors located on a circle $\rho_m^{\nu} = 1.8\,\lambda_0$ in radius belonging to the observation domain. As far as the inversion data are concerned, the values of the scattered field, $E_{scatt}^{v}\left(x_{m_{(v)}}, y_{m_{(v)}}\right)$, have been synthetically computed by using the Richmond's procedure [27]. However, in order to avoid the so-called "inverse crime problem" [28], a different discretization of the investigation domain have been used for the direct procedure.

Figure 3 shows the evolution of the reconstruction obtained by means of the iterative

multi-scaling approach. At the first step ($s = 1$), the investigation domain is partitioned into $N_1 = 36$ square subdomains ($l_2 = 0.4\,\lambda_0$) and the guess dielectric distribution is equal to the background ($\tau = \tau_0$).

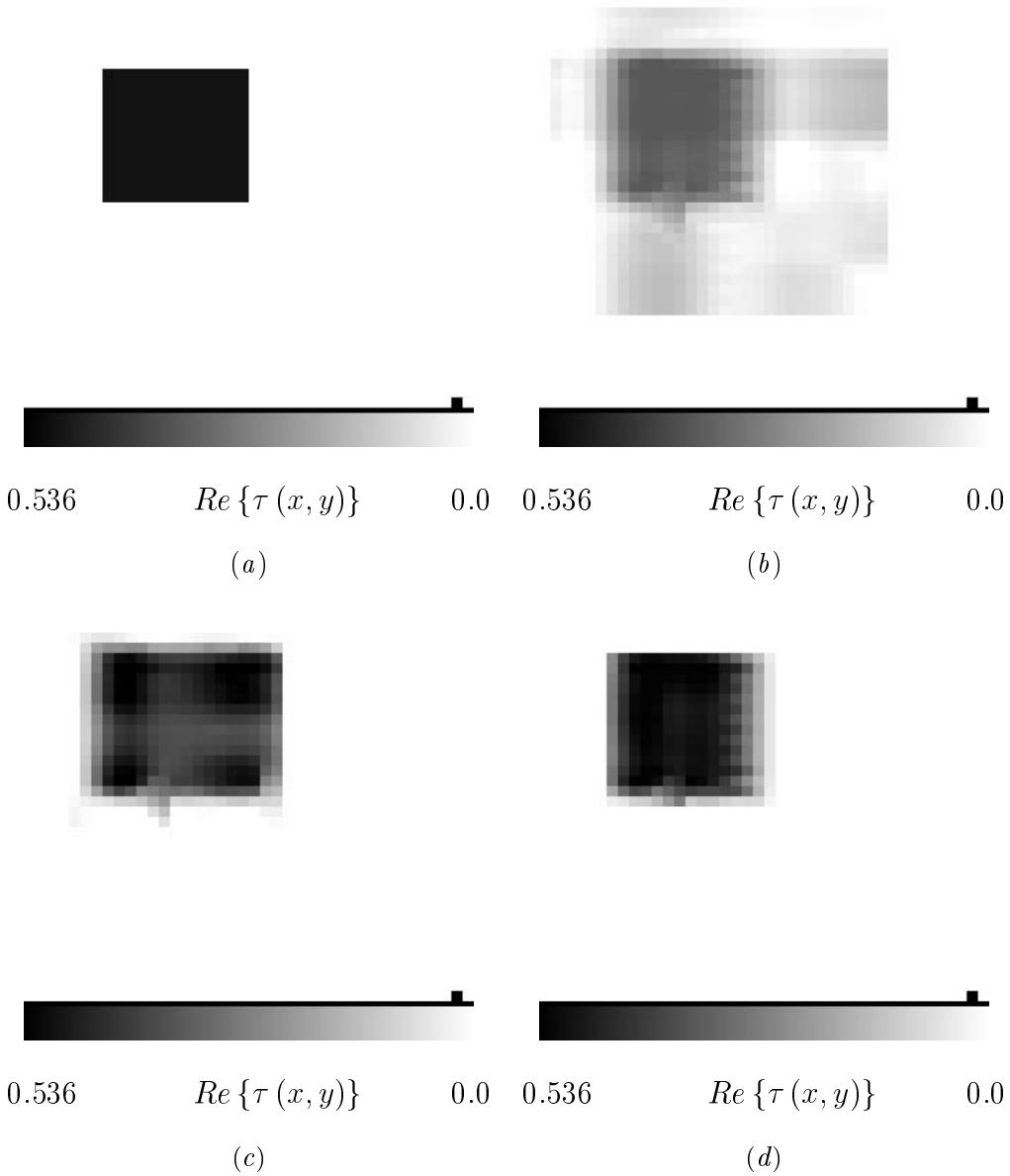

Figure 3. Reconstruction of an off-centered square homogeneous cylinder. (a) Reference distribution. Reconstruction at intermediate steps: (b) $s = 1$, (c) $s = 2$. (c) Final convergent profile ($s = S_{opt} = 3$).

At the end of the minimization process relative to the first step (performed by means of a conjugate-gradient based procedure and stopped when a "stationary condition" in the

decrease of the cost function is achieved (see Fig. 4)), the scatterer is roughly localized ($x_c^{(1)} = -y_c^{(1)} = -0.22\,\lambda_0$) and shaped (Fig. 3($b$)).

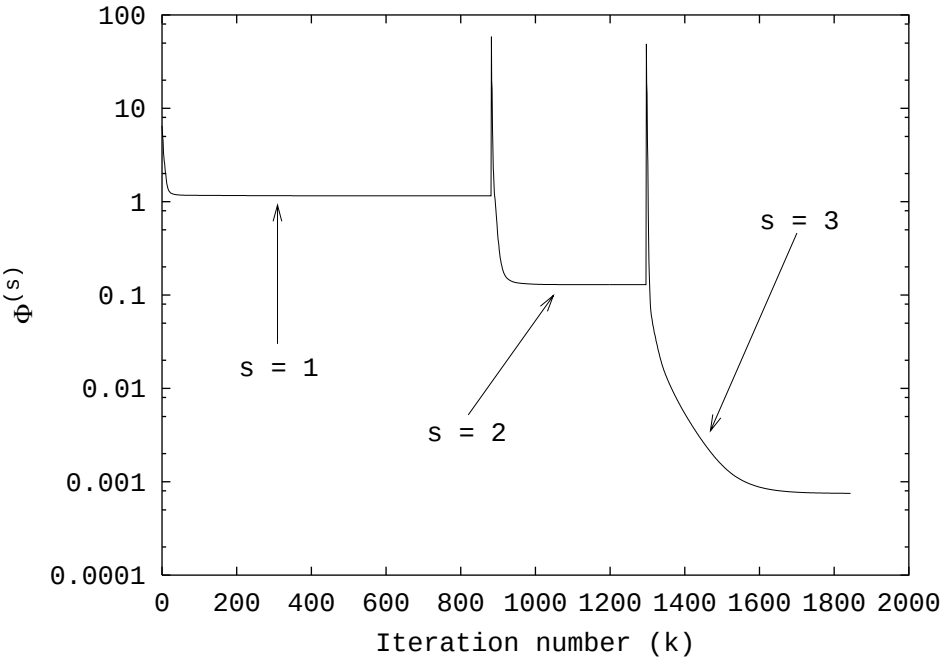

Figure 4. Reconstruction of an off-centered square homogeneous cylinder. Behavior of the multi-resolution cost function.

Then a reduced investigation domain $L_{(1)} = 1.76\,\lambda_0$ in side (Tab. I) is defined.

Step No. (s)	*0*	*1*	*2*	*3*	*4*
$\frac{x_{c_{(s)}}}{\lambda_0}$	0.0	-0.220	-0.380	-0.397	-0.397
$\frac{y_{c_{(s)}}}{\lambda_0}$	0.0	0.220	0.380	0.397	0.397
$\frac{L_{(s)}}{2\lambda_0}$	1.2	0.880	0.540	0.430	0.420

Table I. Reconstruction of an off-centered square homogeneous cylinder. Location and shape parameters.

At the second step two different subgridding are used, the finer resolution is used for the reduced investigation domain found at the previous step. The reduced area is again

discretized into $N_2 = 36$ square subdomains $l_2 = 0.29\,\lambda_0$ in side. Fig 3(c) shows the object profile retrieved at the end of the minimization process of the second step. The multi-scaling iterative procedure is repeated until $s = S_{opt} = 3$ when fixed thresholds (empirically stated and equal to $\eta_x = 1\,\%$, $\eta_y = 1\,\%$, and $\eta_L = 5\,\%$) are reached. The unknown target results correctly located ($x_c^{(3)} = -0.397\,\lambda_0$, $y_c^{(3)} = 0.397\,\lambda_0$) and the occupation area of the actual object estimated with a good accuracy ($L_3 = 0.86\,\lambda_0$). The method provides also a good reconstruction as confirmed from the values of the error figures (Tab. II) which, at the final step, result no greater than 1.5%.

Step No. (s)	*1*	*2*	*3*
γ_{tot}	4.37	0.82	0.12
γ_{int}	11.25	5.80	1.10
γ_{ext}	3.52	0.20	0.01

Table II. Reconstruction of an off-centered square homogeneous cylinder. Error figures.

For the same configuration, the effects of the noise have been taken into account. To this end, a gaussian noise has been added to the data. The noise level ranges from $30\,dB$ up to $5\,dB$. Figure 5 gives a representation of the reconstructed contrast for different signal-to-noise ratio. The final convergent solutions for SNR from $30\,dB$ to $10\,dB$ are reached after 3 scaling steps. Two steps are necessary when $SNR = 5\,dB$. As can be observed, the multi-scaling method appears to be reasonably stable with respect to the noise. It results that only extremely high noise levels yield some anomalies (Figs. 5(c)-5(d)), but the location and the shape of the scatterer are still visible in the reconstructed profile.

As far as the quantitative and qualitative imaging of the scatterer is concerned, some information about the error distribution can be inferred from Figure 6 where the histograms of the behavior of the local error are reported.

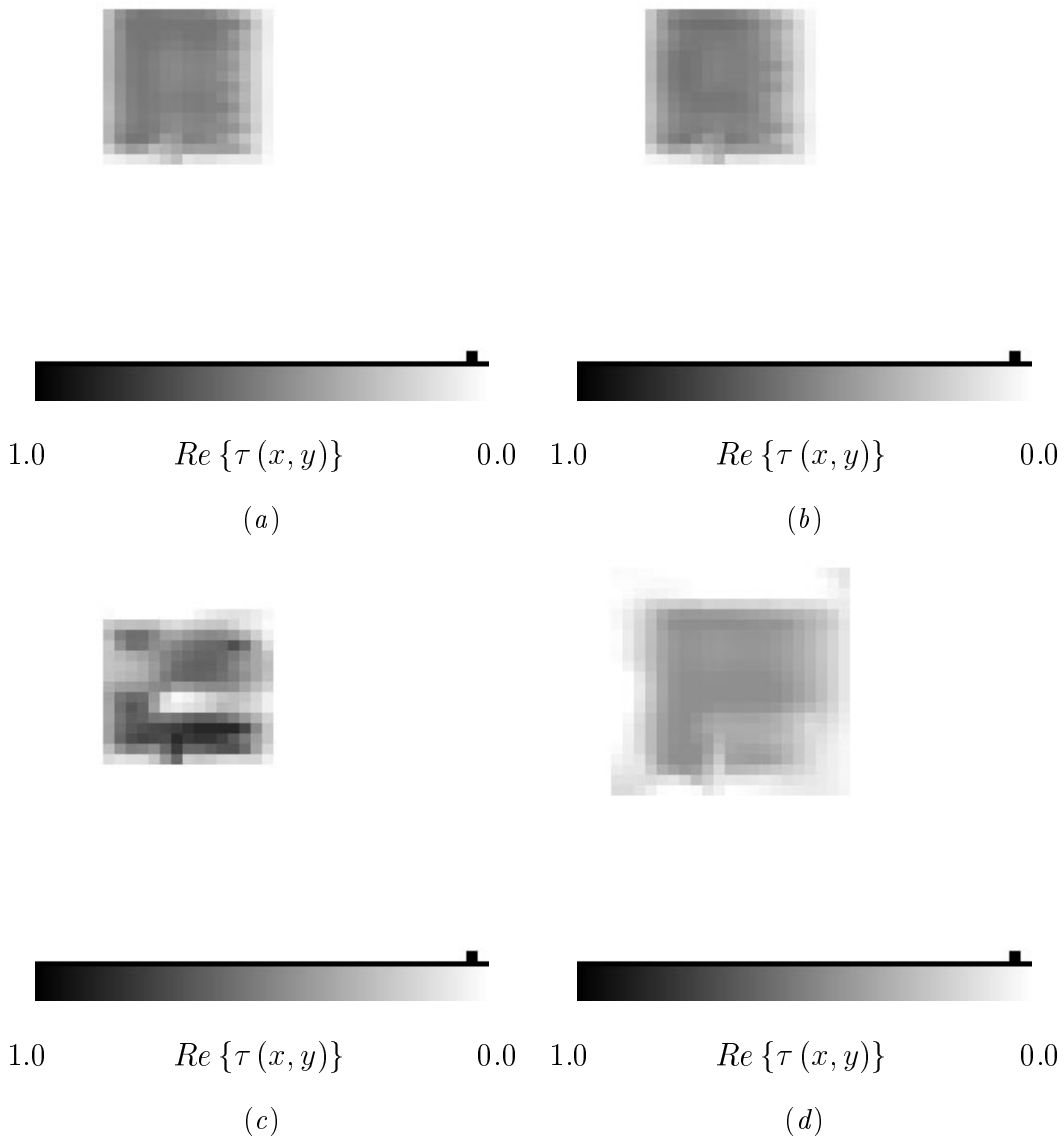

Figure 5. Reconstruction of an off-centered square homogeneous cylinder. Retrieved profiles at $s = S_{opt}$ when SNR is equal to (a) $30\,dB$, (b) $20\,dB$, (c) $10\,dB$, and (d) $5\,dB$.

Each bar of the histogram gives the percentage of cells for which the local error χ (being χ_{tot}, χ_{int} , and χ_{ext} related to the whole scattering domain, inside and outside the object support, respectively) is negligible, between 3 and 10 percent, 10 and 20 percent, and so on. For low noise levels ($SNR > 20\,dB$), about 100% of the cells are without error ($\chi_{tot} \leq 3\,\%$) and the internal local error results lower than 10%. When the signal-to-noise

ratio decreases the local error increases. The quantitative imaging does not result so accurate as confirmed from the gray-level representation given in Fig. 5(c) and 5(d).

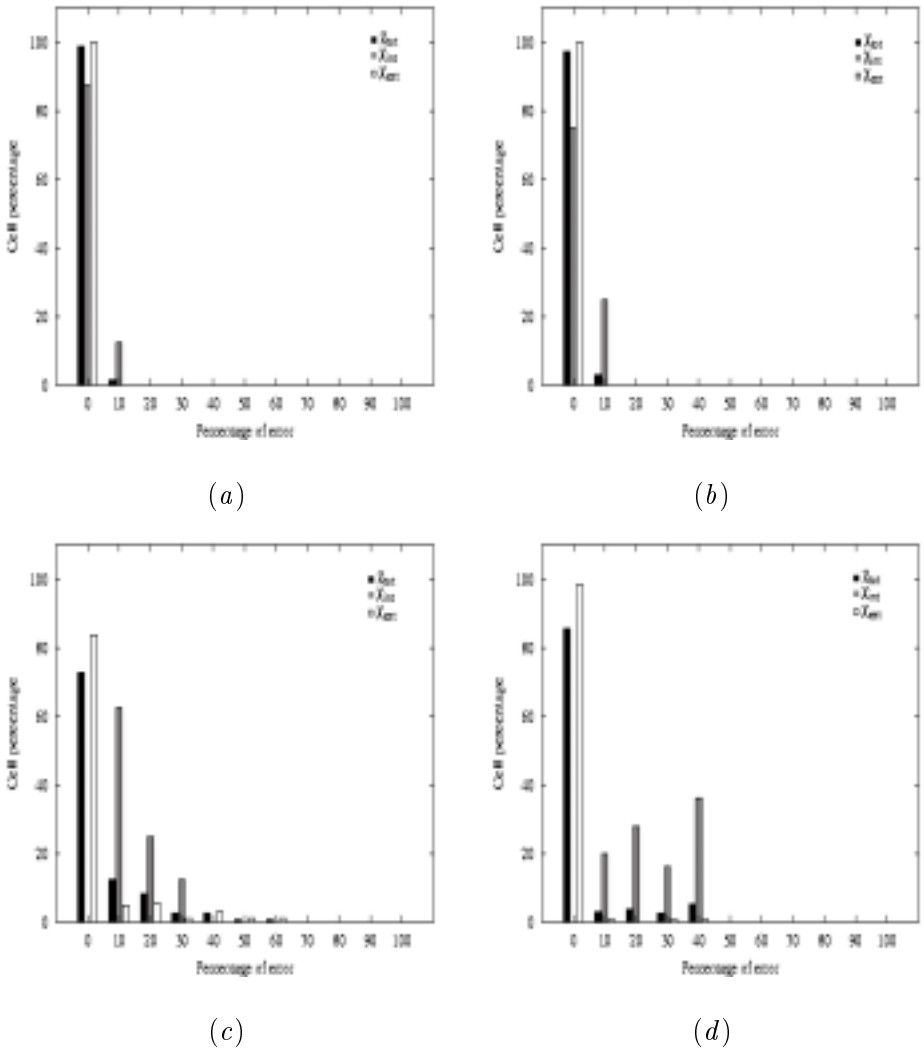

(a) (b)

(c) (d)

Figure 6. Reconstruction of an off-centered square homogeneous cylinder (Noisy data). Local error behavior when (a) $SNR = 100\,dB$, (b) $SNR = 20\,dB$, (c) $SNR = 10\,dB$, (d) $SNR = 5\,dB$.

Almost each cell belonging the area of the actual scatterer is affected by an error. However, the local error is less than 3% in a large amount of the cells outside the scatterer. This further confirms the effectiveness of the multi-resolution procedure in locating and shaping the target under test.

In order to evaluate the effect of the scatterer's dielectric permittivity on the reconstruction process, some simulations have also been performed. To this end, the dimensions and the characteristics of the observation domain have been assumed as those used in the first simulation, while the value of the relative dielectric permittivity of the object has been varied between $\varepsilon_r = 1.2$ and $\varepsilon_r = 3.0$.

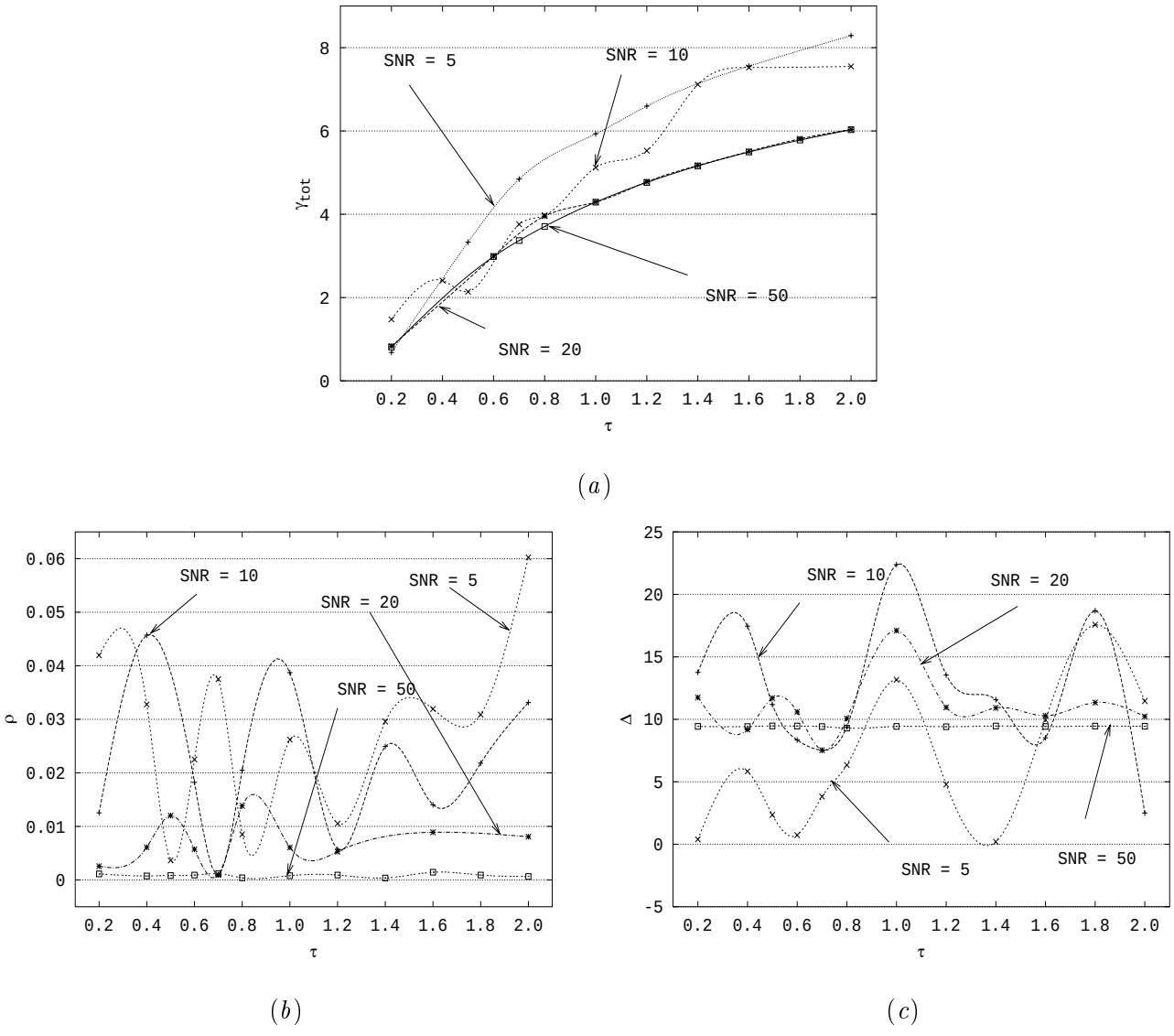

Figure 7. Reconstruction of an off-centered square homogeneous cylinder. Dependence of the (a) reconstruction accuracy, (b) scatterer location, and (c) object shaping from the scatterer's dielectric permittivity.

The quantitative and qualitative imaging capabilities of the proposed procedure can be inferred by observing Fig. 7 where the plots of γ_{tot}, ρ, and Δ are given. As far as the reconstruction of the dielectric profile is concerned, a good accuracy ($\gamma_{tot} \leq 8$) is achieved in the whole range of variations of ε_r and for each signal-to-noise ratio (Fig. $8(a)$). Starting from $Re(\tau) \cong 1.2$, the location error strongly depends on the value of SNR, but in any case ρ results lower than 6 % (Fig. $8(b)$). On the other hand, the error in estimating the occupation area of the scatterer is limited to the range between 5 % and 20 %. It assumes a constant value ($\Delta \cong 9\,\%$) when the measurement environment is characterized by a low noise level ($SNR = 50\,dB$) (Fig. $8(c)$).

To further assess the capabilities of a microwave imaging procedure, it should be taken into account that the size of the object under test could affect the validity of the inversion procedure. Consequently, another set of simulations has been carried out in order to evaluate the suitability of the multi-scaling methodology to deal with smaller as well larger (compared to the background wavelength) scatterers. The area of the square scatterer ($\varepsilon_r = 1.5$) has been varied continuously in the range between $A = 0.1\,\lambda_0^2$ to $A = 2.8\,\lambda_0^2$ and various measurement conditions have been taken into account ($SNR = 0.5 \div 100\,dB$). Figure 8 shows a pictorial representation of the error figures for different values of the scatterer area and for various signal-to-noise ratios. Starting from Fig. $8(a)$, we can observe that when $SNR > 25\,dB$, the reconstruction error is lower than 2 % whatever the object dimensions. On the contrary, when the signal-to-noise increases, γ_{tot} strongly depends to the scatterer area. As an example, assuming $SNR = 10\,dB$, the reconstruction error ranges from 2 % to 10 %. As far as the behavior of ρ is concerned, Fig. $8(b)$ clearly indicates that the method is able to accurately locate the position of the scatterer ($\rho \leq 0.010$ when $SNR \geq 10\,dB$). Generally, also the dimensions of the target are correctly estimated. The occupation area error results equal to $\sim 7.5\,\%$ independently of scatterer's dimensions and noisy conditions.

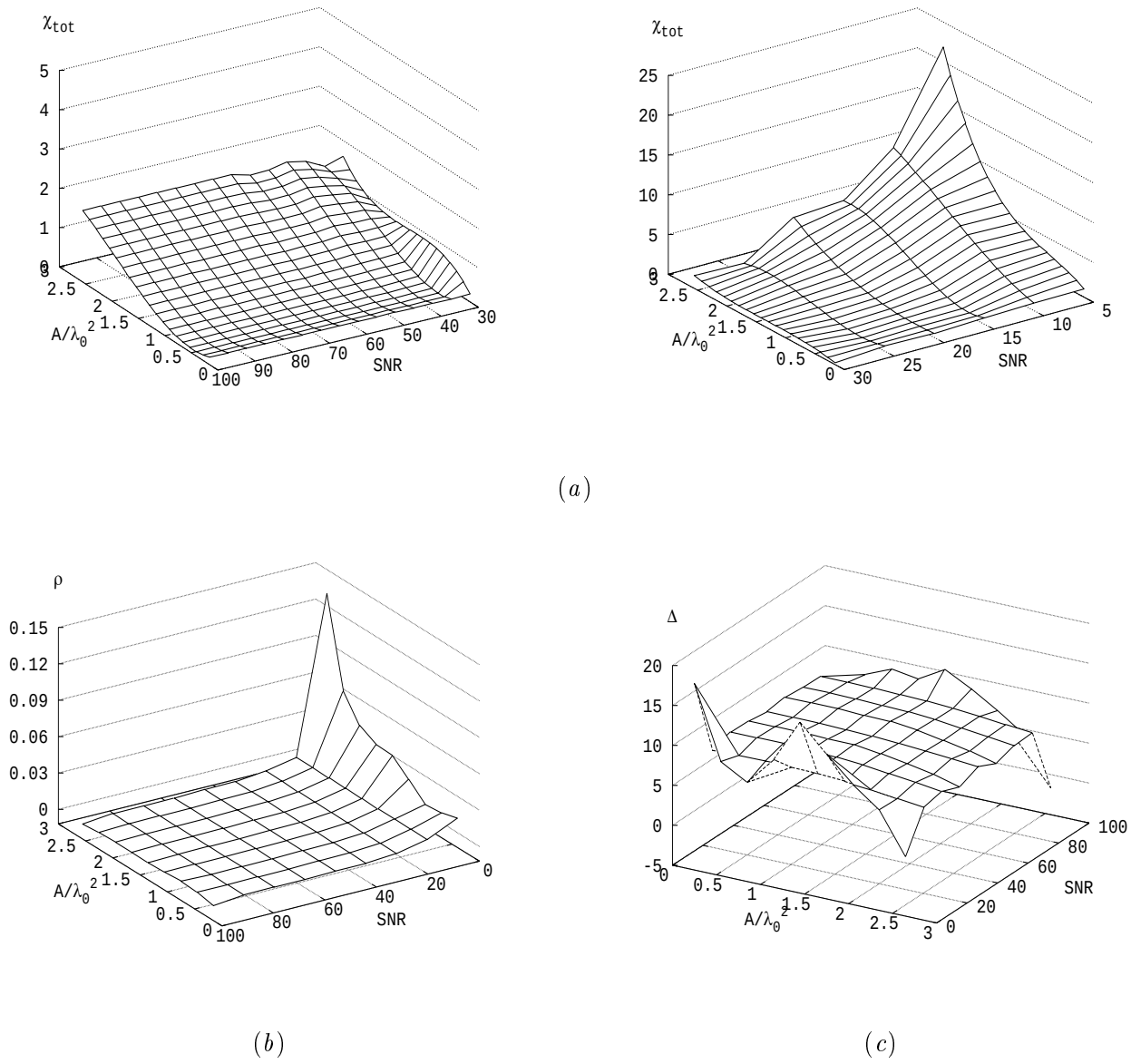

Figure 8. Reconstruction of an off-centered square homogeneous cylinder ($\varepsilon_r = 1.5$). Dependence of the (a) reconstruction accuracy, (b) scatterer location, and (c) object shaping from the scatterer's dimensions.

3.3 Circular Cylinder

In this section, a dielectric profile, for which an analytical solution for the computation of scattered field is available, is considered. An off-centered ($x_c^{ref} = y_c^{ref} = 0.3\,\lambda_0$) circular dielectric cylinder with a relative dielectric permittivity $\varepsilon_r(x, y) = 2.0$, $0.3\,\lambda$ in radius

has been located in the investigation domain. In the first set of numerical simulations, a noiseless environment has been assumed. During the reconstruction process, $Re\{\tau(x,y)\}$ can range between 0.0 and 2.0. Figure 9 shows a grey-level representation of the dielectric distribution of the scatterer under test retrieved at the final step ($S_{opt}=3$) of the multi-resolution procedure. Also the actual distribution is shown (Fig. $9(a)$). As can be observed, the object is correctly located ($x_{c_{(S_{opt})}}=0.301\,\lambda_0$ and $y_{c_{(S_{opt})}}=0.298\,\lambda_0$), shaped ($\frac{L_{(S_{opt})}}{2}=0.324\,\lambda_0$), and reconstructed ($\gamma_{int}=9.022$).

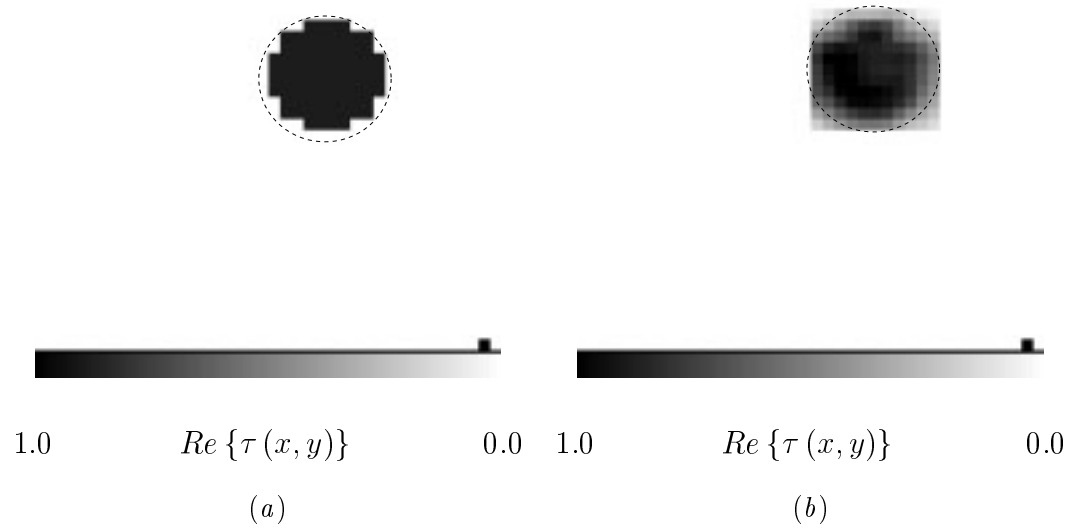

(a) (b)

Figure 9. Reconstruction of a circular homogeneous cylinder (Noiseless conditions). (a) Reference profile and (b) retrieved profile ($s=S_{opt}=3$).

Successively, a gaussian noise characterized by a $SNR=10\,dB$ has been added to the simulated scattered field at the measurement points. Figure 10 shows the reconstructed results at the end of each step of the multi-resolution procedure. The final ($S_{opt}=4$ being $\eta_x^{(4)}<\eta_x$, $\eta_y^{(4)}<\eta_y$, and $\eta_L^{(4)}<\eta_L$) retrieved dielectric profile is reported in Fig. $10(d)$. As expected, the presence of the noise causes a deterioration of the reconstruction accuracy (the maximum value of the dielectric permittivity is estimated to be equal to

$max_{(x,y)\in D}\{\varepsilon_r(x,y)\} = 2.1$), however the values of the error figures (Tab. III) result acceptable also taking into account the high noise level.

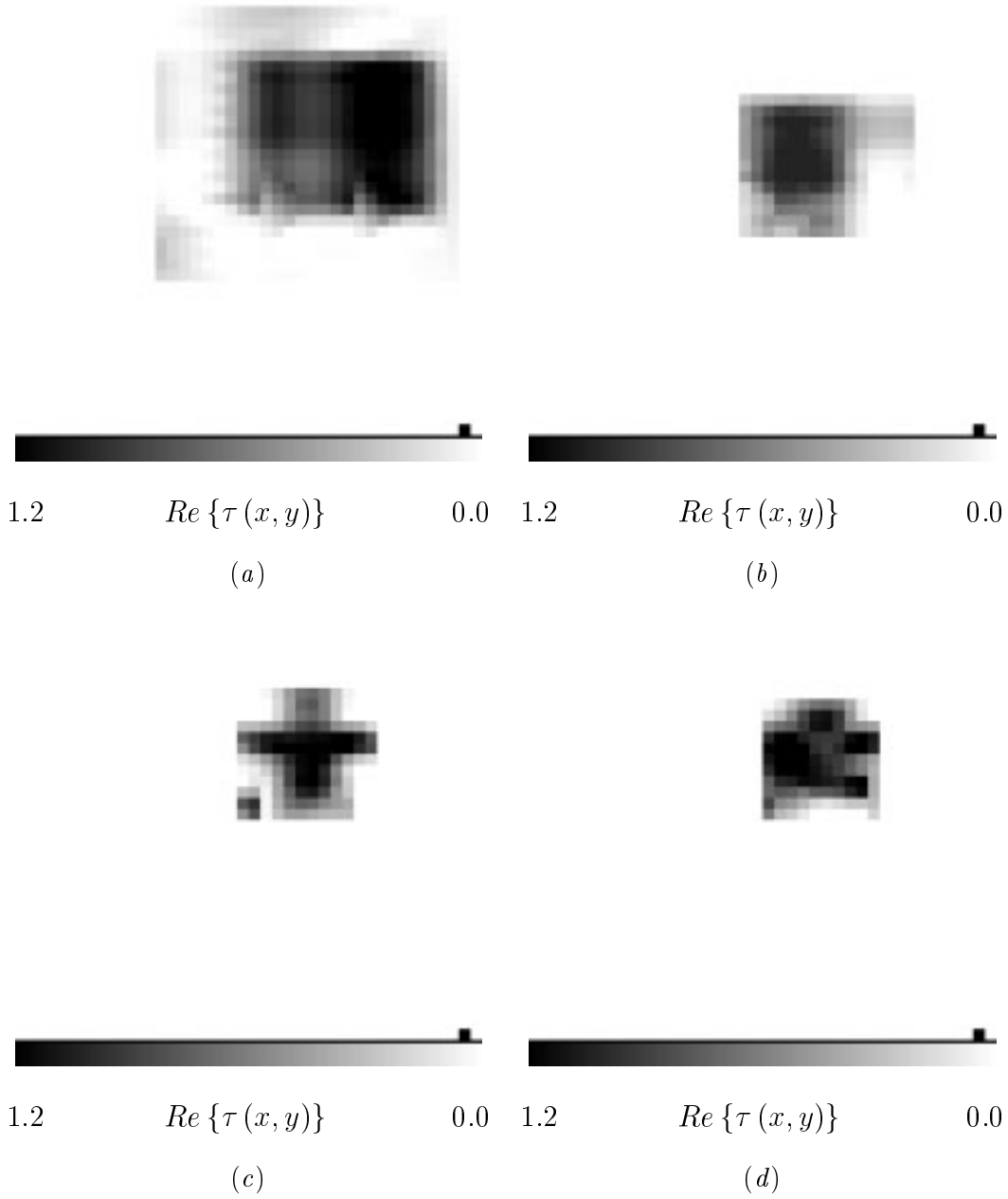

Figure 10. Reconstruction of a circular homogeneous cylinder (Noisy conditions). Reconstruction at intermediate steps: (a) $s = 1$, (b) $s = 2$, (c) $s = 3$. (c) Final convergent profile ($s = S_{opt} = 4$).

Step No. (s)	*1*	*2*	*3*	*4*
$\eta_x^{(s)}$	8.07	4.48	0.098	0.062
$\eta_y^{(s)}$	14.81	0.38	5.84	0.989
$\eta_L^{(s)}$	40.56	21.35	11.33	3.18
γ_{tot}	10.692	4.258	3.477	2.218
γ_{int}	15.295	7.076	13.491	9.202
γ_{ext}	10.535	4.162	3.134	1.979

Table III. Reconstruction of a circular homogeneous cylinder. Behavior of the stationary indexes and error figures.

3.4 Hollow square scatterer

Finally, the reconstruction of a slightly complex cylindrical object is taken into account. The target is an off-centered square two-layered cylinder ($x_c^{ref} = y_c^{ref} - 0.2\lambda_0$). The inner square, characterized by a permittivity equal to that of the background, is $0.4\,\lambda_0$-sided. The side of the outer cylinder ($\tau(x,y) = 0.5$) is equal to $1.2\,\lambda_0$. As far as the noisy environment is concerned, a signal-to-noise ration $SNR = 30\,dB$ has been assumed.
Figure 11 shows the reference and reconstructed object function distribution inside the investigation domain, respectively. As can be noted, the scatterer is accurately localized and quite correctly shaped. However, the side of the square scatterer is slightly overestimated as well as the value of $Re\,(\tau)$ of the inner cylinder. These conclusions are confirmed from the values of the error figures reported in Tab. IV.

On the other hand, when the dimensions of the inner cylinder ($L_{out} = 1.6\,\lambda_0$ and $L_{in} = 0.8\,\lambda_0$) increases also the quality of the reconstruction of the scatterer under test improves (Fig. 12) as confirmed from the error figures (Tab. IV).

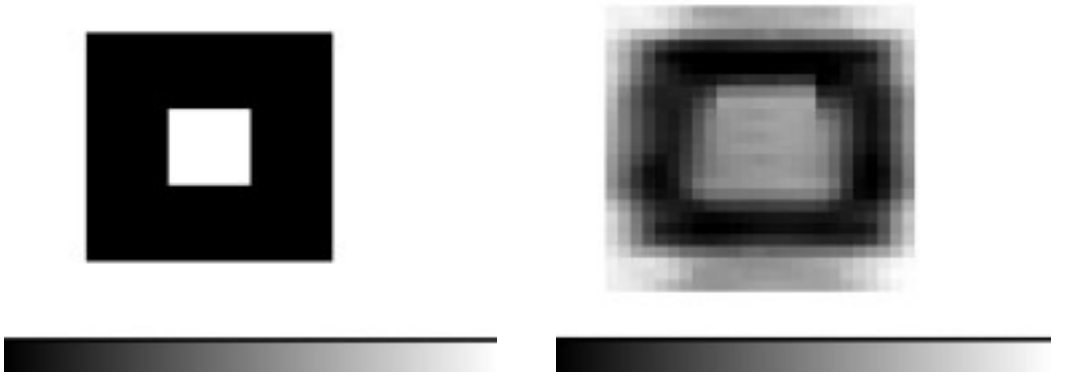

(a) (b)

Figure 11. Reconstruction of a two-layered square cylinder ($L_{out} = 1.2\,\lambda_0$ and $L_{in} = 0.4\,\lambda_0$). (a) Reference profile and (b) retrieved profile ($s = S_{opt} = 3$).

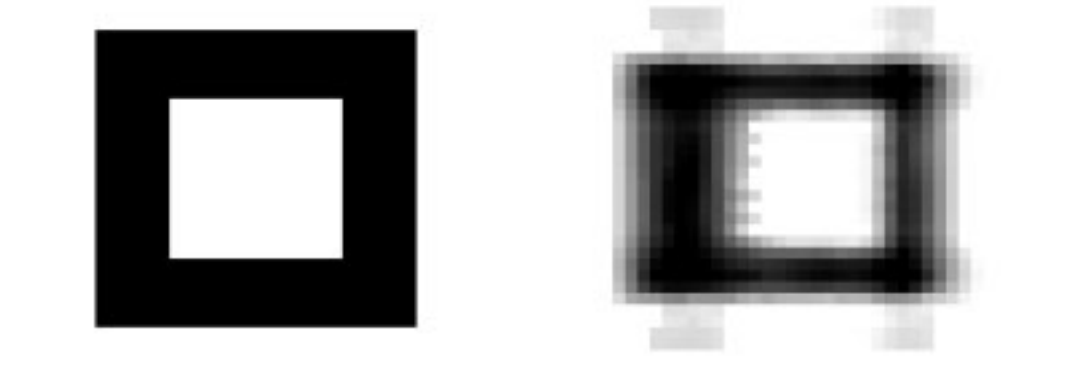

(a) (b)

Figure 12. Reconstruction of a two-layered square cylinder ($L_{out} = 1.6\,\lambda_0$ and $L_{in} = 0.8\,\lambda_0$). (a) Reference profile and (b) retrieved profile ($s = S_{opt} = 4$).

	Two-layered Square Cylinder	
	$L_{out} = 1.2\,\lambda_0$ - $L_{in} = 0.4\,\lambda_0$	$L_{out} = 1.6\,\lambda_0$ - $L_{in} = 0.8\,\lambda_0$
γ_{tot}	5.961	4.640
γ_{int}	12.150	5.017
γ_{ext}	4.316	1.39

Table IV. Reconstruction of two-layered square cylinders. Error figures.

4 Conclusions

An innovative methodology for reconstructing the dielectric permittivity distribution of cylindrical scatterers has been presented. The procedure, based on a multi-level resolution algorithm, is aimed at better exploit the limited amount of the information achievable from the scattering measurement. To this end, a suitable iteratively defined (according to the information about the scatterer collected at the previous steps) cost function is successively minimized by means of an optimization method. A conjugate-gradient based method has been used, but, in principle, any kind of optimization technique could be successfully adopted.

The proposed approach, developed in the spatial domain and under TM illumination conditions, has been assessed by means of some test cases and the obtained results have shown its capabilities in imaging simple objects, even in strongly noisy environments. In more detail, numerical simulations have been carried out to test the behavior of the multi-resolution procedure when some parameters (e. g., scatterer dimensions, dielectric permittivity, scatterer shapes, etc .) of the scenario under test are changed. Results are quite promising, however, the proposed scheme must be further improved by overcoming some current limitations. In particular, at the present, a modified version is under development in order to improve the imaging performance by including in an efficient way all

the available *a-priori* information.

References

[1] W. Tabbara, B. Beuchene, C. Pichot, D. Lesselier, L. Chommeloux and N. Joachimowicz, "Diffraction tomography: contribution to the analysis of applications in microwave and ultrasonics," *Inverse Problems*, vol. 4, pp. 305-331, 1988.

[2] D. Colton and R. Krees, *Inverse acoustics and electromagnetic scattering theory.* Berlin, Germany: Springer-Verlag, 1992.

[3] M. Bertero, E. R. Pike, *Inverse problems in scattering and imaging.* Bristol: Adam Hilger 1992.

[4] T. M. Habashy, M. L. Oristaglio and A. T. de Hoop, "Simultaneous non linear reconstruction of two-dimensional permittivity and conductivity," *Radio Sci.*, vol. 29, pp. 1101-1118, 1994.

[5] J. C. Bolomey et al., "Microwave diffraction tomography for biomedical applications," *IEEE Trans. Microwave Theory Tech.,* vol. MTT-30, pp. 1998-2000, 1982.

[6] A. K. Louis, "Medical imaging: State of the art and future development," *Inverse Problems,* vol. 8, pp. 709-738, 1992.

[7] R. L. Barbour, M. J. Carvlin and M. A. Fiddy, *Experimental and numerical methods for Solving ill-posed inverse Problems: medical and non medical applications.* Eds. San Diego, CA, 1995.

[8] S. R. H. Hoole et al., "Inverse problem methodology and finite elements in the identifications of cracks, sources, materials, and their geometry in inaccessible locations," *IEEE Trans. Magn.*, vol. 27, pp. 3433-3443, 1991.

[9] A. C. Dubey et al., *Detection technology for mines and minelike targets*. Eds. Orlando, FL, 1995.

[10] K. M. Golden et al., "Inverse electromagnetic scattering models for sea ice," *IEEE Trans. Geosci. remote Sensing*, vol. 36, pp. 1675-1704, 1998.

[11] A. Quing and L. Jen, "Microwave imaging of dielectric cylinder in layered media," *J. Electromagn. Waves Applicat.,* vol. 11, no. 2, pp. 259-269, 1997.

[12] J. C. Bolomey, "Recent European developments in active microwave imaging for industrial, scientific and medical applications," *IEEE Trans. Microwave Theory Tech.*, vol. 4, pp. 305-331, 1988.

[13] B. D. Steinberg, *Microwave imaging techniques*. New York: Wiley, 1991.

[14] A. Kirsch, *An introduction to the mathematical theory of inverse problems*. New York: Springer-Verlag, 1996.

[15] A. M. Denisov, *Elements of theory of inverse problems*. Utrecht, The Netherlands: VSP, 1999.

[16] D. Colton, L. Paivarinta, "The uniqueness of a solution to an inverse scattering problem for electromagnetic waves," *Arc. Rational Mech. Anal.*, 119, pp 59-70, 1992.

[17] V. Isakov, "Uniqueness and stability in multidimensional inverse problems," *Inverse Problems*, vol. 9, pp. 579-621, 1993.

[18] M. Slaney, A. C. Kak, and L. E. Larsen, "Limitations of imaging with first-order diffraction tomography," *IEEE Microwave Theory Tech.*, vol. 32, pp. 860-874, 1984.

[19] R. E. Kleinman and P. M. Van den Berg, "A modified gradient method for two-dimensional problems in tomography," *J. Comput. Appl. Math.*, vol. 42, pp. 17-35, 1992.

[20] W. C. Chew and Y. M. Wang, "Reconstruction of two-dimensional permittivity distribution using the distorted Born iterative method," *IEEE Trans. Medical Imaging*, vol. 9, pp. 218-225, 1990.

[21] L. Garnero, A. Franchois, J.-P. Hugonin, Ch. Pichot, and N. Joachimowicz, "Microwave imaging-Complex permittivity reconstruction by simulated annealing," *IEEE Trans. Microwave Theory Tech.*, vol. 39, pp. 1801-1807, 1991.

[22] A. Massa, "Genetic algorithm based techniques for 2D microwave inverse scattering," in *Recent Research Developments in Misrowave Theory and Techniques*, Ed. S. G. Pandalai, Transworld Research Network Press, Trivandrum, India, 2002, (*in press*).

[23] M. Pastorino, A. Massa and S. Caorsi, "A microwave inverse scattering technique for image reconstruction on a genetic algorithm," *IEEE Trans. Measurement and Instrumentation*, vol. 49, 2000.

[24] M. Bertero, C. De Mol, and E. R. Pike, "Linear inverse problems with discrete data. I: General formulation and singular system analysis," *Inverse Problems*, vol. 1, pp. 301-330, 1995.

[25] M. Bertero and P. Boccacci, *Introduction to Inverse Problems in Imaging.* IOP Publishing Ltd, Bristol, 1998.

[26] Ch. Pichot, P. Lobel, C. Dourthe, L. B. Féraud, and M. Barlaud, "Microwave inverse scattering: quantitative reconstruction of complex permittivity for different applications", *IEICE Trans. Electron.*, vol. E80-C, pp. 1343-1348, 1997.

[27] J. H. Richmond, "Scattering by a dielectric cylinder of arbitrary cross section shape," *IEEE Trans. Antennas Propagat.*, vol. 13, pp. 334-341, 1965.

[28] D. Colton and R. Kress, *Inverse Acoustic and Electromagnetic Scattering Theory.* Springer, Berlin, 1992.

[29] K. Belkebir, R. E. Kleinman, and C. Pichot, “Microwave imaging location and shape reconstruction from multifrequency scattering data,” *IEEE Trans. Microwave Theory Tech.*, vol. 45, pp. 469-476, 1997.

[30] H. Harada, D. J. N. Wall, T. T. Takenaka, and T. Tanaka, “Conjugate gradient method applied to inverse scattering problems,” *IEEE Trans. Antennas Propagat.*, vol. 43, pp. 784-792, 1995.

[31] L. Garnero, A. Franchois, J.-P. Hugonin, Ch. Pichot, and N. Joachimowicz, “Microwave imaging - Complex permittivity reconstruction by simulated annealing,” *IEEE Trans. Microwave Theory Tech.*, vol. 39, pp. 1801-1807, 1991.

[32] S. Caorsi, A. Massa, M. Pastorino, "A computational technique based on a real-coded genetic algorithm for microwave imaging purposes," *IEEE Trans. Geoscience and Remote Sensing*, special issue on "Computational Wave Issues in Remote Sensing, Imaging and Target Identification, Propagation, and Inverse Scattering," vol. 38, n. 4, part I, pp. 1697-1708, July 2000.